AAPT PHYSICS EDUCATION | AMERICAN JOURNAL of PHYSICS

Experiments with a Malkus–Lorenz water wheel: Chaos and Synchronization

Lucas Illing, Rachel F. Fordyce, Alison M. Saunders, and Robert Ormond

Citation: Am. J. Phys. **80**, 192 (2012); doi: 10.1119/1.3680533
View online: http://dx.doi.org/10.1119/1.3680533
View Table of Contents: http://ajp.aapt.org/resource/1/AJPIAS/v80/i3
Published by the American Association of Physics Teachers

Experiments with a Malkus–Lorenz water wheel: Chaos and Synchronization

Lucas Illing,[a] Rachel F. Fordyce, Alison M. Saunders, and Robert Ormond
Physics Department, Reed College, Portland, Oregon 97202

(Received 13 May 2011; accepted 11 January 2012)

We describe an experimental implementation of the Malkus–Lorenz water wheel. We demonstrate that both chaotic and periodic behavior is observed as wheel parameters are changed in agreement with predictions from the Lorenz model. We further show that when the measured angular velocity of the water wheel is used as an input signal to a computer model implementing the Lorenz equations, high-quality synchronization of the model and the water wheel is achieved in the chaotic regime. This indicates that the Lorenz equations provide a good description of the water wheel dynamics. © *2012 American Association of Physics Teachers.*
[DOI: 10.1119/1.3680533]

I. INTRODUCTION

Ever since Edward Lorenz discovered that a simple three-variable set of ordinary differential equations can give rise to exceedingly complex behavior,[1] the study of chaos has continued unabated. Over the years, chaos has been found in a variety of naturally occurring systems and many experiments have been conducted to quantitatively study the different aspects of this phenomenon. These experiments have included such diverse systems as dripping faucets,[2] pendula,[3] chemical reactions,[4] and lasers.[5]

For practical applications, optical and electronic chaotic systems operating on time scales of nanoseconds or less represent one current area of research.[5–8] Yet for the purpose of gaining intuition, chaotic mechanical systems operating on time scales of seconds are unsurpassed because of their palpable mechanisms and the direct experience they provide. A prime example of such an experiment is the Malkus–Lorenz waterwheel, slowly rotating one way and then the other in a calming yet interestingly unpredictable fashion.

The chaotic waterwheel was first envisioned and constructed by Malkus and coworkers in the 1970s as a mechanical analogue of the Lorenz equations.[9,10] It has fascinated both students and teachers and has become particularly well known since its discussion in Steven Strogatz's introductory text on nonlinear dynamics.[11] The Malkus waterwheel described in this paper was inspired by this discussion and became the focus of a senior thesis project of one of the authors (Rachel Fordyce).

The most basic Malkus waterwheel consists of a few leaking cups attached to the rim of a freely turning wheel, whose axis may be either horizontal or tilted. A single stream of water at the top of the wheel will add water whenever a cup is close to the top. Although the motion of such a simple waterwheel can be analyzed,[12] its dynamics differs from that of the Lorenz model. We refer to such a waterwheel as non-ideal. The goal in our experiment was to construct an ideal waterwheel, one whose dynamics is accurately described by the Lorenz equations.

In this paper, we aim to evaluate how close we have come to this goal. In Sec. II, we present the details of our experiment, with a focus on confirming three crucial assumptions that are made in deriving the Lorenz equations from the wheel's dynamics. The derivation of the mathematical model and a brief overview of some of its properties are presented in Sec. III. Experiments resulting in both chaos and periodic oscillations are shown in Sec. IV. In an effort to make a more precise statement regarding the match of model and experiment, we turn in Sec. V to an analytic proof and the experimental demonstration of synchronized chaos. Finally, we conclude with a discussion in Sec. VI.

II. EXPERIMENTAL SETUP

In designing our water wheel, we strove to balance the desire for a simple and inexpensive experiment and our goal to come as close as possible to an ideal waterwheel. Three properties of an ideal waterwheel require consideration. First, the amount of water entering the cups per unit time has to be constant, which means that gaps between the cups and cup overflow must be avoided. Second, damping needs to be entirely due to frictional torque proportional to the angular velocity (viscous damping), which means that dry friction (kinetic and static) has to be negligible in the experiment. And third, the cup leakages should be proportional to the water mass in a cup, which suggests that the outflowing water should exit through a pipe with a laminar flow described by the Hagen–Poiseuille equation. With these requirements in mind, a waterwheel was constructed as described below.

A relatively small (16.5-in.) BMX bicycle wheel was used for the wheel. It was chosen for its smooth bearings that guaranteed very low axle friction. The wheel was mounted to a pair of hinged boards, enabling us to vary the inclination angle α of the wheel with respect to the horizontal (see Fig. 1).

Fifty-six plastic syringes (50 cm^3) served as leaking "cups" and were attached to the perimeter of the wheel using a metal synching band. For each syringe, the sides of the finger pull were shaved off in order to allow a snug fit with no gap between the syringes. Subsequent to attaching the syringes, the wheel was balanced with small weights so the angle at which an empty tilted wheel would come to a stop was unbiased. We found that this balancing was necessary to remove the wheel's tendency to preferentially stop with its welding seam at the bottom.

The motion of the wheel was detected using a rotary encoder attached to the wheel's hub. Its output pulses were counted continuously by an interface circuit containing a HCTL-2016 quadrature decoder and counter chip that includes a 16-bit memory for storage. The counts on the memory chip were then acquired by a computer with a 10-Hz sampling rate for the data shown in this paper.

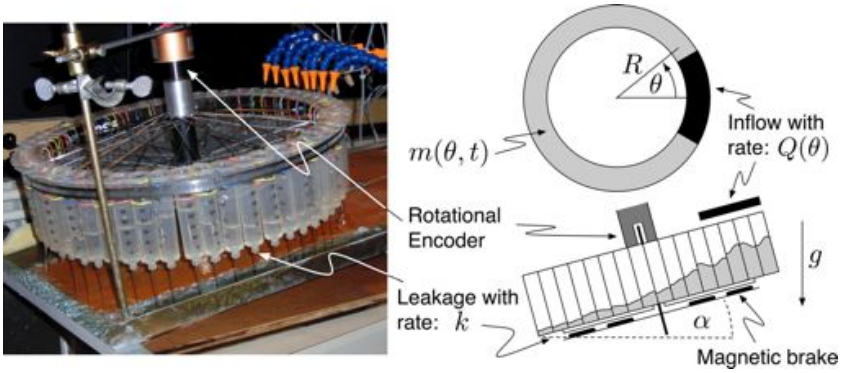

Fig. 1. (Color online) Experimental implementation of the Malkus–Lorenz water wheel, constructed using a bicycle wheel, syringes, and rare earth magnets forming a magnetic brake. The schematics on the right show a side view (bottom) and a top view (top) of the wheel. (See text for details.)

A magnetic braking system was employed to achieve viscous damping as follows. A (non-magnetic) Aluminum disk was attached below the wheel such that it co-rotates with the wheel. A second non-rotating disk with the same radius and several rare-earth magnets glued to its surface were mounted coaxially to the first disk. When the wheel is in motion, the stationary magnets induce eddy currents in the spinning disk to oppose any changes in magnetic flux. The result is a damping torque that is directly proportional to the angular velocity.[13–15] The gap between the two disks, and, therefore, the damping coefficient, is tunable in our setup.

To check whether the damping torque in our wheel is linear in the velocity, we measured the rotational position (θ) of the rotating wheel without water as a function of time and fitted the results. To obtain a model for the fit, we assume that the only relevant torques are from viscous friction due to the magnets and kinetic friction. The magnetic brake contributes a torque $\boldsymbol{\tau}_{\mathrm{vf}} = -\kappa\boldsymbol{\omega}$, where κ is the viscous friction parameter and $\boldsymbol{\omega}$ is the angular velocity.[16] The magnitude of the kinetic friction force is $F_{\mathrm{kf}} = \mu F_{\mathrm{N}}$, where μ is the friction coefficient and F_N is the normal force. Since F_N can be taken as constant and the setup is rotationally symmetric, the torque due to kinetic friction is a constant ($|\boldsymbol{\tau}_{\mathrm{kf}}| = \tau_{\mathrm{kf}} = \text{const.}$) opposing the motion of the wheel. The evolution of the magnitude of the angular velocity is, therefore, described by the first-order ordinary differential equation

$$I_{\mathrm{wh}}\frac{d\omega}{dt} = -\kappa\omega - \mathrm{sgn}(\omega)gt\tau_{\mathrm{kf}}, \tag{1}$$

where I_{wh} is the moment of inertia of the wheel with the attached empty syringes. Equation (1) can be integrated, without loss of generality, under the assumption that $\omega(t=0) = \omega_0 > 0$, yielding

$$\omega(t) = -\frac{\tau_{\mathrm{kf}}}{\kappa} + \left(\omega_0 + \frac{\tau_{kf}}{\kappa}\right)e^{-(\kappa/I_{\mathrm{wh}})t}, \tag{2}$$

for $t \le t_{\mathrm{stop}}$. The magnitude of the angular velocity decreases in time and, once it reaches zero at time $t = t_{\mathrm{stop}}$, the wheel stops because the torques due to viscous and kinetic friction are zero and static friction implies that some finite minimal torque has to be applied to set the wheel in motion again. Integration of Eq. (2) yields the experimentally measurable angle $\theta(t)$ as a function of time ($t \le t_{\mathrm{stop}}$)

$$\theta = -\frac{\tau_{\mathrm{kf}}}{\kappa}t + \frac{I_{\mathrm{wh}}}{\kappa}\left(\omega_0 + \frac{\tau_{\mathrm{kf}}}{\kappa}\right)\left(1 - e^{-(\kappa/I_{\mathrm{wh}})t}\right), \tag{3}$$

where we have taken $\theta(0) = 0$. A convenient parameterization is achieved by introducing the viscous damping rate $\gamma = \kappa/I_{\mathrm{wh}}$ and kinetic friction parameter $\Omega = \tau_{\mathrm{kf}}/\kappa$, yielding

$$\theta = -\Omega t + \frac{\omega_0 + \Omega}{\gamma}(1 - e^{-\gamma t}). \tag{4}$$

In Fig. 2, we show two fits of the data: a three-parameter fit corresponding to Eq. (4) and a two-parameter fit that corresponds to Eq. (4) with damping entirely due to viscous friction ($\Omega = 0$). Figure 2(a) demonstrates that both fits provide an excellent description of the data—they are essentially indistinguishable to the eye. The effect of kinetic friction is only noticeable when the wheel is turning very slowly. As shown in Fig. 2(b), the residuals for both fits scatter around a value of zero for the first 4 s, indicating that both models provide a good fit. However, when the angular velocity is small, the residuals show a non-random deviation from zero. In particular, the residuals of the last 2 s before the wheel comes to a stop demonstrate that the two-parameter model slightly overestimates the angle. Despite this, these results clearly indicate that damping is dominated by the magnetic brake and that our waterwheel comes close to the ideal where damping is entirely due to viscous friction. To keep the model as simple as possible, we, therefore, neglect kinetic friction and set $\tau_{\mathrm{kf}} = 0$.

The wheel's moment of inertia can be determined by performing a second measurement and two parameter fit [Eq. (4) with $\Omega = 0$] where a known set of additional weights of total mass m is attached symmetrically to the wheel's rim.[17] Using

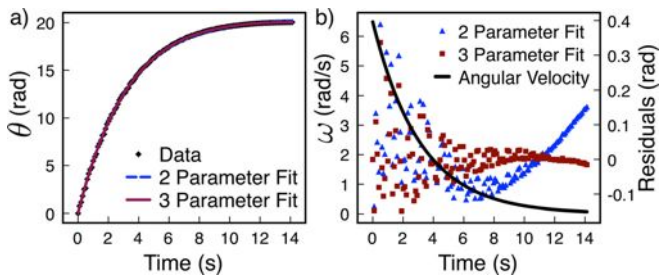

Fig. 2. (Color online) Measurements of angle versus time for an empty wheel are compared with fits that take into account damping due to viscous friction (two-parameter fit) and a combination of viscous and kinetic friction (three-parameter fit). (a) Angle-data and fits. (b) Residuals of fits (triangles and squares) and angular velocity ω as determined from the two-parameter fit (solid line).

the new fitted viscous damping rate $\tilde{\gamma} = \kappa/(I_{\rm wh} + mR^2)$, the previously determined γ, and the relation

$$I_{\rm wh} = mR^2 \frac{\tilde{\gamma}}{\gamma - \tilde{\gamma}}, \tag{5}$$

We found that our wheel has a moment of inertia of $I_{\rm wh} \approx 0.11\,{\rm kg\,m^2}$.

For an ideal waterwheel, it is important that the inflow is symmetric with respect to the centerline that divides the wheel into left and right. To achieve this symmetry while minimizing the probability of cup overflow for sufficient inflow rates, we use a system of eight individually adjustable spigots.[18] The spigots were placed symmetrically with respect to the top, spanning angles $\theta \in [-\theta_0, +\theta_0]$ with $\theta_0 \approx 26°$. A uniform distribution of (incoming) mass flux, described by

$$Q(\theta) = \begin{cases} 0 & \theta \in [-\pi, \theta_0) \\ \dfrac{Q_{\rm tot}}{2\theta_0} & \theta \in [-\theta_0, \theta_0], \\ 0 & \theta \in (\theta_0, \pi] \end{cases} \tag{6}$$

was ensured by verifying experimentally that for a stationary wheel all eight top cups fill at identical rates. The total mass flux $Q_{\rm tot}$ was measured using a digital flow meter[19] and was tunable with a range of 0.03–0.09 kg/s.

Finally, the ideal wheel should have a leakage rate that is proportional to the water mass. Because we use syringes as "cups," water leaks out through the small cylindrical nozzles at the end of the syringes, suggesting a theoretical description of laminar flow of a viscous fluid through the pipe. One can even attach needles to the syringes to increase the length of the pipe. If laminar pipe flow of the exiting water is the dominant effect, one expects the total volume V of water in the syringe (radius $r_{\rm c} = 1.08\,{\rm cm}$) to be governed by the Hagen–Poiseuille equation[20]

$$\frac{dV}{dt} = -\frac{\pi r_{\rm p}^4}{8\nu\rho_{\rm w}}\left(\frac{\Delta P}{z_p}\right). \tag{7}$$

Here, $r_{\rm p}$ is the exit pipe radius, while $\rho_{\rm w}$ and ν are the density and kinematic viscosity of water, respectively. ΔP is the difference in modified pressure over the length of the exit pipe z_p. Modified pressure is defined as $P(z) \equiv p(z) + \rho_w g z$, where $p(z)$ is the pressure as a function of the position z within the vertical exit pipe; the term $\rho_w g z$ arises due to the force of gravity acting on the water contained within the pipe.[20] Because the pressure difference between the pipe's bottom and top is $\Delta p = \rho g(h + \ell - z_p)$ [see Fig. 3(c)], the difference in the modified pressure is $\Delta P = \rho g(h + \ell)$. The total volume $V = \pi r_{\rm c}^2 h + V_{\rm b}$ consists of the water in the cylindrical part of the syringe and an additional $\sim 2\,{\rm cm}^3$ volume $V_{\rm b}$ at the bottom. From Eq. (7), we then find that the volume of water in the syringe obeys

$$\frac{dV}{dt} = -\frac{r_{\rm p}^4 g}{8\nu r_{\rm c}^2 z_{\rm p}}\left[\pi r_{\rm c}^2 (h + \ell)\right] = -k(V + V_{\rm off}), \tag{8}$$

where $V_{\rm off} = \pi r_{\rm c}^2 \ell - V_{\rm b}$ is a constant offset term, and k is a fit parameter, nominally given by $k = r_{\rm p}^4 g/(8\nu r_{\rm c}^2 z_p)$. The fit model is obtained by integrating Eq. (8) to get

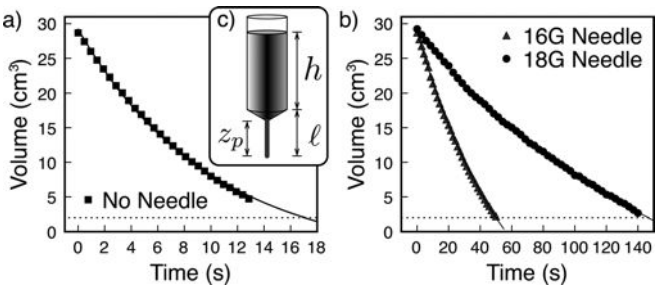

Fig. 3. Measurements of the water volume in the syringe as a function of time and the two-parameter fit of Eq. (10). The dotted line indicates the value of V_b (see text). (a) Syringe without needle ($V_{\rm off} = 4\,{\rm cm}^3$). Fit-result: $V_0 = 29\,{\rm cm}^3$, $k = 0.10\,{\rm s}^{-1}$ (b) Syringe with needles ($V_{\rm off} = 18\,{\rm cm}^3$) of 16 gauge (Fit-result: $V_0 = 29\,{\rm cm}^3$, $k = 0.017\,{\rm s}^{-1}$) and 18 gauge (Fit-result: $V_0 = 29\,{\rm cm}^3$, $k = 0.006\,{\rm s}^{-1}$). (c) Geometry of the syringe, consisting of a cylindrical main body (radius r_c, height h), a tapered section, and either a nozzle or a needle as exit "pipe" (radius r_p, height z_p). The total height of the tapered section and exit "pipe" is ℓ.

$$V(t) = V_0 e^{-kt} + V_{\rm off}(e^{-kt} - 1). \tag{9}$$

This model is valid for water levels within the cylindrical part of the syringe, i.e., for $V(t) > V_{\rm b}$. The drainage of the small bottom volume cannot be measured with our setup, but we are expecting it to deviate somewhat from Eq. (9) due to the tapering of the syringe and capillary effects. However, since the bottom volume is quite small, we expect only very minor corrections that we neglect from our analysis.

To check the validity of Eq. (9), we measure the declining water volume in a vertical syringe as a function of time using digital video analysis. The experiment is performed with and without needles attached to the syringe. As shown in Fig. 3, the fit is already quite accurate for the syringe without needle [Fig. 3(a)] and becomes even better when a needle is attached [Fig. 3(b)]. Note that by attaching needles and by changing the gauge of the needles, the leakage rate k can be varied by orders of magnitude. No needles were attached for the data shown in this paper.

Writing Eq. (8) in terms of the total mass of water in all 56 syringes ($M_{\rm tot} = 56\rho_{\rm w} V$), and accounting for the incoming water by introducing an effective mass flux

$$Q_{\rm eff}(\theta) = Q(\theta) - \frac{56k\rho_{\rm w} V_{\rm off}}{2\pi}, \tag{10}$$

where $Q(\theta)$ is given by Eq. (6), one finds that the total mass in the wheel evolves according to

$$\frac{dM_{\rm tot}}{dt} = -kM_{\rm tot} + Q_{\rm eff}^{\rm tot}, \tag{11}$$

with $Q_{\rm eff}^{\rm tot} = Q_{\rm tot} - 56k\rho_{\rm w} V_{\rm off}$. Equation (11) shows that the total mass of water is conserved in the asymptotic limit because $M_{\rm tot} = Q_{\rm eff}^{\rm tot}/k$ for $t \to \infty$.

III. MATHEMATICAL MODEL

To make this paper self-contained, we recall here the well known derivation of the equations describing the dynamics of the water wheel and briefly discuss the parameter dependence of the model solutions.

A. Derivation

In our derivation we follow Strogatz[11] and model the water as being distributed as a continuous ring around the rim of the wheel. Matson[17] showed that the same result can be obtained when considering an ideal water wheel with a discrete set of cups.

In the continuum approximation, the mass distribution $m(\theta,t)$ around the wheel's rim is defined such that the mass between the angles θ_1 and θ_2 (fixed in the lab frame) is

$$M(t) = \int_{\theta_1}^{\theta_2} m(\theta,t)d\theta. \tag{12}$$

The change in time of $m(\theta, t)$ is given by

$$\frac{\partial m(\theta,t)}{\partial t} = Q_{\text{eff}}(\theta) - km(\theta,t) - \omega(t)\frac{\partial m(\theta,t)}{\partial \theta}. \tag{13}$$

In this equation, the constant inflow $Q(\theta)$, described by Eq. (6), contributes to the first term. The leakage, which is proportional to the water mass, results in the second term but also contributes a constant offset to the inflow that results in Q_{eff} defined by Eq. (10). The third term takes into account the wheel's rotation. It expresses the fact that for a wheel without water inflow and leakage rotating with angular velocity ω, the mass density at angle θ and time $t+\Delta t$, i.e., $m(\theta,\ t+\Delta t) \approx m(\theta,\ t) + \partial m(\theta,\ t)/\partial t \cdot \Delta t$, is identical to the mass density at time t at angle $\theta - \Delta\theta$, i.e., $m(\theta-\Delta\theta,\ t) \approx m(\theta, t) - \partial m(\theta, t)/\partial\theta \cdot \Delta\theta$.

The change in time of the angular velocity is due to the applied total torque, which has three components. As discussed in Sec. II, the magnetic brake contributes $\tau_{\text{vf}} = -\kappa\omega(t)$. The infalling water contributes a torque $\tau_{\text{spin up}} = -Q_{\text{tot}} R^2\omega(t)$, corresponding to the change in angular momentum that arises because water enters the wheel a distance R from the center with zero angular velocity while at the same instance an equivalent amount of water leaks out with angular velocity ω. Gravity provides the third torque because each infinitesimal mass element $m(\theta,\ t)d\theta$ on a wheel that is tilted at an angle α contributes

$$d\tau_{\text{grav}} = Rg\sin(\alpha)\sin(\theta)m(\theta,t)d\theta. \tag{14}$$

Taken together, one obtains

$$I_{\text{tot}}\frac{d\omega(t)}{dt} = -\left(\kappa + Q_{\text{tot}}R^2\right)\omega(t) + Rg\sin(\alpha)\int_{-\pi}^{\pi} m(\theta,t)\sin(\theta)d\theta, \tag{15}$$

where we have taken I_{tot} to be constant. As described in conjunction with Eq. (11), the assumption that I_{tot} is constant is valid after an initial transient, i.e., after the total water mass has come exponentially close to its final constant value.

Since $m(\theta,\ t)$ is periodic in θ, one can expand this function into Fourier-modes as

$$m(\theta,t) = \sum_{n=1}^{\infty} a_n(t)\sin(n\theta) + \frac{b_0(t)}{2} + \sum_{n=1}^{\infty} b_n(t)\cos(n\theta). \tag{16}$$

Under the assumption that $Q(\theta)$ is truly symmetric with respect to the wheel's center line, the effective inflow Q_{eff} can be written as

$$Q_{\text{eff}}(\theta) = \frac{q_0}{2} + \sum_{n=0}^{\infty} q_n\cos(n\theta) - \frac{56}{2\pi}k\rho_{\text{w}}V_{\text{off}}, \tag{17}$$

with coefficients

$$q_n = \frac{Q_{\text{tot}}}{\pi}\text{sinc}(n\theta_0) \quad (n = 0, 1, 2, \ldots), \tag{18}$$

for the case that $Q(\theta)$ is given by Eq. (6). Substituting these series into Eqs. (13) and (15) and equating the coefficients of each harmonic separately, one obtains an infinite set of ordinary differential equations that describes the evolution of the angular velocity $\omega(t)$ and the Fourier-mode amplitudes $a_n(t)$ and $b_n(t)$. Amazingly, the evolution of the angular velocity and amplitudes $a_1(t)$ and $b_1(t)$ is entirely decoupled from the evolution of all other amplitudes. In other words, the angular velocity can be found simply from a_1 and b_1, even though all (infinitely many) Fourier-mode amplitudes are required to determine the complete mass distribution. Therefore, the problem is reduced to a three-dimensional system of ordinary-differential equations

$$\begin{aligned}
\frac{d\omega}{dt} &= -\frac{\kappa + Q_{\text{tot}}R^2}{I_{\text{tot}}}\omega(t) + \frac{\pi Rg\sin\alpha}{I_{\text{tot}}}a_1(t)\\
\frac{da_1}{dt} &= -ka_1(t) + \omega(t)b_1(t)\\
\frac{db_1}{dt} &= q_1 - kb_1(t) - \omega(t)a_1(t).
\end{aligned} \tag{19}$$

It turns out that Eq. (19) can be mapped onto the Lorenz equations by introducing the dimensionless parameters

$$\sigma = \frac{1}{k}\frac{\kappa + Q_{\text{tot}}R^2}{I_{\text{tot}}}, \quad \rho = \frac{q_1}{k^2}\frac{\pi Rg\sin\alpha}{\kappa + Q_{\text{tot}}R^2}, \tag{20}$$

the dimensionless time $s = kt$, and the coordinates

$$x = \frac{\omega}{k}, \quad y = \frac{\rho k}{q_1}a_1, \quad z = \rho - \frac{\rho k}{q_1}b_1. \tag{21}$$

In the new coordinates, Eq. (19) becomes

$$\begin{aligned}
\dot{x} &= \sigma(y - x)\\
\dot{y} &= \rho x - y - xz,\\
\dot{z} &= xy - z
\end{aligned} \tag{22}$$

where the overdot denotes the derivative with respect to dimensionless time s. The coupled equations given in Eq. (22) are identical to the Lorenz equations with the third parameter—the coefficient of z in the third equation, often denoted as b —equal one.

The above mapping of the problem onto Eq. (22) relies in an essential way on the fact that Eq. (13) is linear in $m(\theta,\ t)$. This explains why the leakage in an ideal waterwheel must be proportional to the water mass. Furthermore, to obtain the correct form of the Lorenz system, Eq. (15) must be linear in $\omega(t)$, making a purely viscous damping a principal requirement of ideal waterwheels.

B. Characterization via Lyapunov exponents

Starting with Lorenz's seminal 1963 paper,[1] the Lorenz equations have been studied intensively over many decades. It turns out that this simple looking deterministic system has an extremely rich set of dynamical behaviors. For some parameter values, the asymptotic solutions are steady-state solutions; other values give periodic oscillations.[11,21] But the reason the Lorenz equations are famous is that for a wide range of parameter values, the solutions exhibit chaotic behavior. They oscillate irregularly, never exactly repeating, and depend very sensitively on the choice of initial conditions. Although some rigorous results have been derived for the Lorenz system,[21–24] such results are challenging to obtain. Therefore, one generally resorts to approximate numerical calculations to characterize solutions.

To numerically classify solutions of Eq. (22) as a function of the parameters, we compute the largest Lyapunov exponents. Lyapunov exponents provide a useful classification measure because they are independent of the particular initial conditions used to compute them and are invariant under smooth nonsingular coordinate transformations such as those in Eq. (21). In addition, they directly measure a distinguishing characteristic of chaotic solutions, their "sensitivity to initial conditions." For chaotic systems, small differences in initial conditions yield after an exponentially short time widely diverging solutions, rendering impossible the long-term prediction of outcomes from finite-precision measurements of initial states. Roughly speaking, two trajectories in phase space with initial separation $\delta\mathbf{x}_0$ diverge as

$$|\delta\mathbf{x}(t)| \approx e^{\lambda t}|\delta\mathbf{x}_0|, \tag{23}$$

where λ, the largest Lyapunov exponent (LLE), is a positive real number for a chaotic system that characterizes the exponential rate of growth. In contrast, stable steady-state solutions have a negative LLE, because perturbations away from the steady state decay exponentially, and stable periodic solutions have a LLE with value zero, because perturbations along a trajectory neither grow nor shrink in time (perturbations perpendicular to the trajectory decay exponentially). Thus, solutions to the Lorenz equations can be classified as being chaotic, periodic, or steady state based on the sign of the LLE.

Figure 4 depicts the results of a numerical calculation of the LLEs on a 156×200 grid of (ρ, σ) parameter values, providing a map of the water wheel's dynamic behavior as a function of ρ and σ. (Details about the numeric calculation are given in Appendix A.) It is seen that for small values of either parameter only negative LLEs are found (green and blue colors), corresponding to steady state behavior of the angular velocity. For larger parameter values, the wheel exhibits either chaotic or periodic behavior. We find that there exist large continuous regions with a zero LLE (shown in white), corresponding to periodic behavior. In addition, there are large continuous regions with positive LLEs (shown in red and yellow), corresponding to chaos. Interestingly, the numerical calculations reveal that there are periodic windows embedded inside the chaotic region and that these windows seem to form a fractal set, with an increasing number of ever smaller periodic windows, each organized along a line in parameter space. This intricate structure means that the qualitative dynamics of the Lorenz system depends very sensitively on the chosen parameter values.

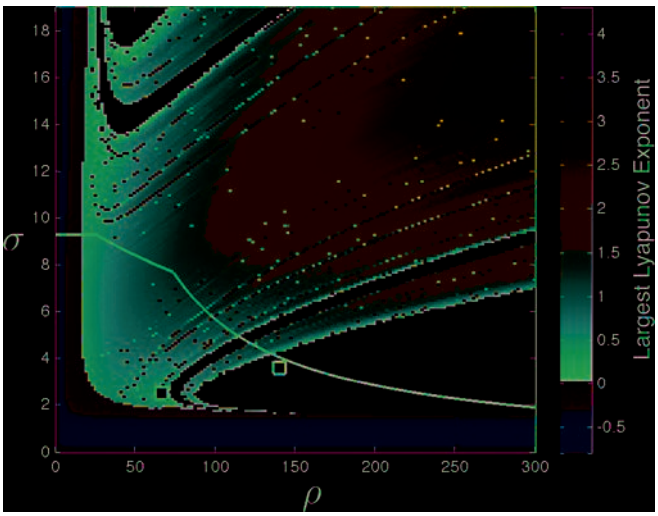

Fig. 4. Numerically determined largest Lyapunov exponent as a function of ρ and σ. White corresponds to a zero exponent implying periodic oscillation of ω. Red colors correspond to positive and blue colors to negative exponents, indicating, respectively, chaos and steady state evolution of ω. The approximate upper boundary of the experimentally accessible region is shown by the solid black line. The yellow squares indicate parameter values corresponding to the chaotic and periodic experimental time series in Fig. 5.

It also should be noted that for some parameter values several different asymptotic solutions (i.e., attractors) may coexist in phase space.[21] Our results only depict the LLE associated with one of those solutions, the one whose basin of attraction includes the randomly chosen initial condition of the simulation.

IV. EXPERIMENTAL CHAOS

Figure 4 is a useful guide for the experiments because it informs our choice of wheel parameters that result in a desired dynamic behavior. This *a priori* connection between the wheel operating condition and expected dynamic behavior is possible because we can explicitly write the parameters ρ and σ as a function of the experimentally tunable and fixed measurable parameters. Leaving aside the option of attaching needles to the wheel, the experimentally adjustable parameters are the inclination angle α, the viscous damping rate γ, and the total mass flux Q_{tot}. We obtain ρ and σ in terms of these quantities by substituting Eq. (18) for q_1, writing $I_{\text{tot}} = I_{\text{wh}} + M_{\text{tot}}R^2 = I_{\text{wh}} + Q_{\text{eff}}^{\text{tot}}R^2/k$, and using $\kappa = \gamma I_{\text{wh}}$. These substitutions yield

$$\sigma(Q_{\text{tot}}, \gamma) = \frac{\gamma I_{\text{wh}} + Q_{\text{tot}}R^2}{kI_{\text{wh}} + Q_{\text{tot}}R^2 - 56k\rho_{\text{w}}V_{\text{off}}R^2}, \tag{24}$$

$$\rho(Q_{\text{tot}}, \gamma, \alpha) = \frac{Q_{\text{tot}}Rg\,\text{sinc}(\theta_0)\sin(\alpha)}{k^2(\gamma I_{\text{wh}} + Q_{\text{tot}}R^2)}. \tag{25}$$

One useful fact, made apparent by these equations, is that one can tune the parameter ρ independently of σ by varying the wheel's inclination angle α. Moreover, we can determine the portion of parameter space that can be accessed with our implementation of the water wheel. The accessible region's approximate upper boundary is shown in Fig. 4 by the black solid line.

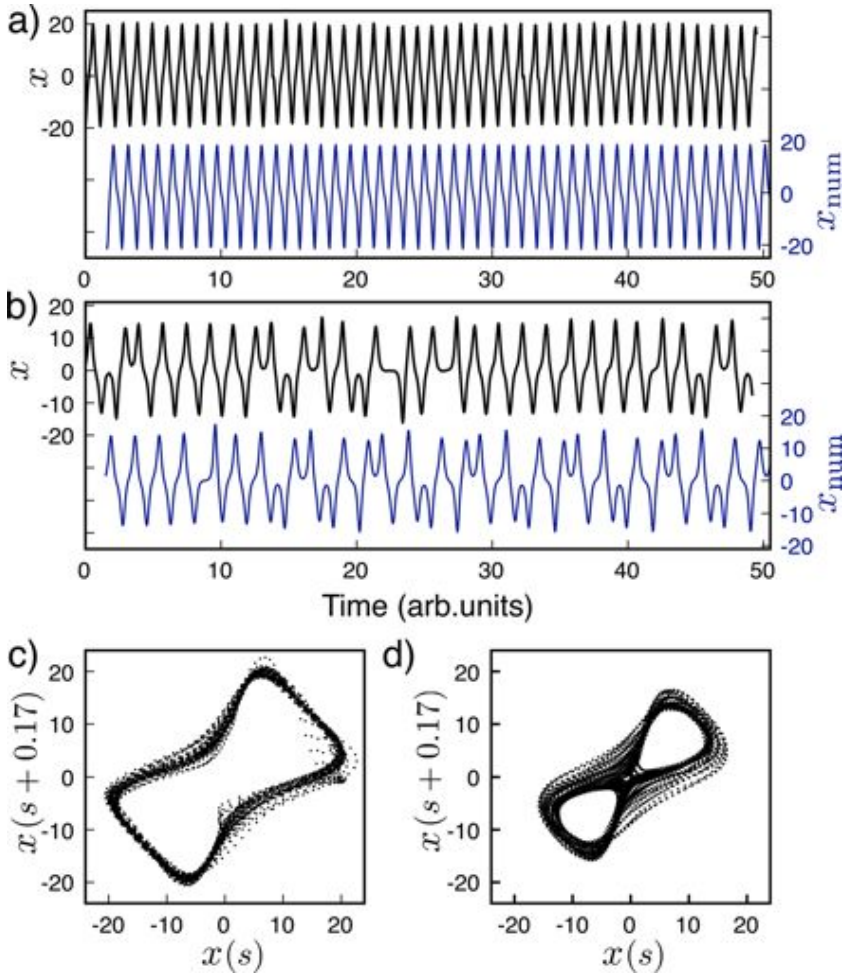

Fig. 5. (Color online) (a) and (b) The experimental time series of the rescaled angular velocity $x=\omega/k$ as a function of the dimensionless time $s=kt$ is shown as the upper trace, and the corresponding numerical solution x_{num} as the lower trace. The parameters are (a) $\sigma\approx 3.6$ and $\rho\approx 140$, resulting in periodic oscillations, and (b) $\sigma\approx 2.5$ and $\rho\approx 66$, resulting in chaotic oscillations. A corresponding two dimensional time-delay embedding of the experimental data is shown in (c) for the periodic and (d) for the chaotic case.

Due to the experimental limitations such as noise and parameter drift, it is not possible to resolve the fine fractal structure seen in Fig. 4 experimentally. Nevertheless, we find that our waterwheel qualitatively conforms to the theoretical predictions. For small ρ or σ it shows steady state behavior of the angular velocity, corresponding to either stationary behavior or rotation with constant speed. For larger parameter values, we find chaos or periodic oscillations. Furthermore, for fixed values of $\sigma\approx 3$, we find that the wheel is in a steady state for very small angles α (small ρ), becomes chaotic when noticeably tilted and exhibits periodic behavior for large angles α (large ρ).

As an example of our experimental data, we display in Fig. 5 two time series, one periodic [Fig. 5(a)] and one chaotic [Fig. 5(b)], corresponding to the parameter values indicated by the two yellow squares in Fig. 4. For each run, we record the wheel's angle θ as a function of time for several hours. The first hour (approximately) is discarded as transient and the rest is used for further analysis. Next, we both low-pass filter and take the first derivative of the data in the Fourier-domain. Working in the Fourier domain is an efficient way of suppressing high frequency noise that would otherwise dominate the derivative. It is a legitimate way of proceeding because the data are highly oversampled (on the order of 100 points per oscillation period) and the Fourier spectrum has a dominant (but broadened) peak even for chaotic time series, which enables us to choose a filter that has essentially no effect at dynamically relevant time-scales. For example, the angle data corresponding to the chaotic time series in Fig. 5(b) are peaked around 0.07 Hz and the filter cutoff was chosen at ~0.6 Hz. Having computed the angular velocity ω, we use the coordinate transformation (21) to obtain $x=\omega/k$.

The upper traces in Fig. 5 are approximately 7 min windows of data obtained after processing the data. The time trace in Fig. 5(a) is clearly periodic. The small fluctuations of the amplitude are a result of the unavoidable imperfections of the experiment. These fluctuations become even more apparent in the two dimensional projection of phase space shown in Fig. 5(c), which is obtained via time-delay embedding[25,26] of the same scalar data that were used to generate Fig. 5(a). An ideal noise-free experiment exhibiting periodic oscillations should result in a single closed loop (a limit cycle), whereas our data result in a smeared-out loop. Nevertheless, the correspondence between the experiment and theory is quite good as can be seen in Fig. 5(a) by comparing the experimental data (upper) with the numerical solution (lower) using the same parameter values (see square in white region in Fig. 4).

Contrary to the data in Fig. 5(a), the time series in Fig. 5(b) is not periodic. A time-delay embedding of this data is depicted in Fig. 5(d) and shows a complicated (potentially

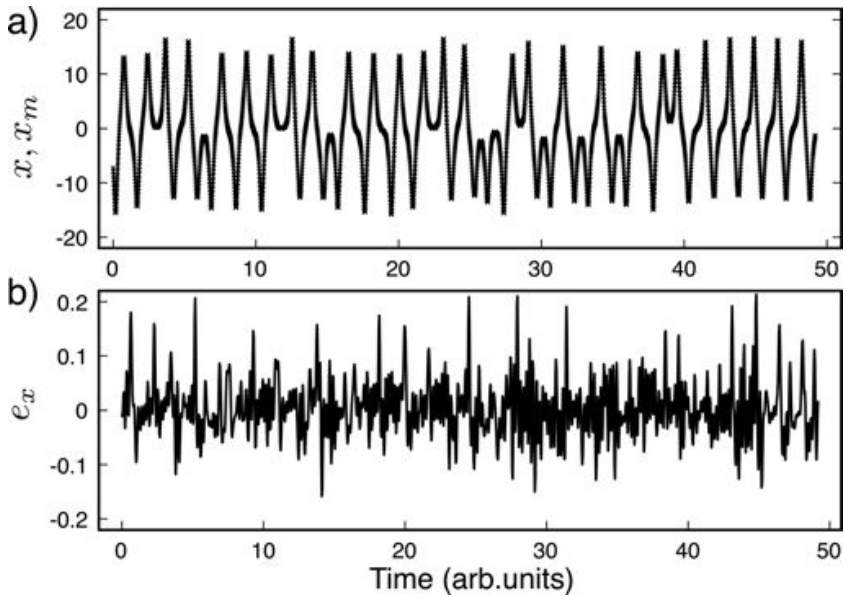

Fig. 6. (a) Experimental time-series (solid line) and model output (crosses). (b) Difference between model and experiment.

fractal) attractor. Taken together, these data indicate that the wheel oscillates chaotically. For comparison, we also display in Fig. 5(b) the result of a simulation of the Lorenz equations with the corresponding parameter values of ρ and σ, which lie in the chaotic regime of the model (see square in red region in Fig. 4). Again, we find a convincing qualitative correspondence between the experiment and theory in the sense that amplitude, dominant frequency, and general character of the solutions match. Since the solutions are chaotic they are, of course, not expected to be identical.

So far, we have demonstrated good qualitatively agreement between the observed waterwheel behavior and the predictions of the Lorenz equations. In order to obtain a more precise statement about the correspondence between theory and the experiment, we turn to another fascinating aspect of nonlinear dynamics: synchronized chaos.

V. SYNCHRONIZED CHAOS

Though the synchronization of clocks (periodic systems) has been studied with great care over centuries,[27] the discovery that two chaotic oscillators could synchronize came as a surprise.[28] Synchronization was unexpected because sensitivity to small perturbations means that the solutions of two chaotic systems tend to diverge. However, it was found that if two chaotic systems are coupled to each other in a suitable way, it is possible for one chaotic system to precisely follow the time evolution of another (identical) chaotic system, even if the two systems start from very different initial conditions. Indeed, for the Lorenz system one can prove that this is the case (see Appendix B).

The phenomenon of chaos synchronization suggests the following test of the validity of the Lorenz equations as a description of the waterwheel. If the waterwheel dynamics are described by the Lorenz equations, then a computer model should synchronize to the waterwheel for a suitably chosen coupling. In particular, consider a setup where we measure the angular velocity of the water wheel as a function of time, thereby determining $x(t)$ in Eq. (22), and use this data as input to a numerical Lorenz model given by

$$\begin{aligned} \dot{x}_\mathrm{m} &= \sigma(y_\mathrm{m} - x_\mathrm{m}) - K(x_\mathrm{m} - x) \\ \dot{y}_\mathrm{m} &= \rho x_\mathrm{m} - y_\mathrm{m} - x_\mathrm{m} z_\mathrm{m} \\ \dot{z}_\mathrm{m} &= x_\mathrm{m} y_\mathrm{m} - z_\mathrm{m}, \end{aligned} \tag{26}$$

where K is the coupling parameter setting the coupling strength. It can be shown (Appendix B) that for coupling parameter values K larger than an explicitly determined sufficient value [Eq. (B6)], two Lorenz systems coupled unidirectionally, as described by Eq. (26), will identically synchronize. Therefore, if no synchronization is observed when the experimental data are used, then the water wheel dynamics is not accurately modeled by the Lorenz equations.

It is important to emphasize that systems often synchronize for smaller coupling strengths than the one obtained in the proof because Eq. (B6) is a sufficient, and generally rather conservative, lower bound on K. It should also be noted that, in the $K \to \infty$ limit, the model output x_m will converge to any given input x, independent of the form of the dynamical system that generated x. In other words, the convergence of x_m to input x does not prove the correctness of the Lorenz model. However, if x_m does not converge to a (noise-free) input x for the sufficient coupling strength K given by Eq. (B6), then x is definitely not generated by a system that evolves according to the Lorenz equations.

When coupling the chaotic data, part of which is shown in Fig. 5(b), to the Lorenz model (26) using a coupling strength of $K = 2260$ suggested by Eq. (B6), we find high-quality synchronization. In fact, we find that the model synchronizes to the data for much lower values of K. An example is shown in Fig. 6(a) where we display the experimental data and model output for a coupling strength of $K = 100$ and find that they are indistinguishable to the eye. The difference between model and experiment $e_x = x_m - x$, is shown in Fig. 6(b). This "error" has a magnitude around 1% of the oscillation amplitude and is of much higher frequency than the natural timescale of the chaos. Such a high frequency is consistent with the interpretation that noise in the data is the main source of the error.

The fact that synchronization takes place for the coupling strength (B6) and, as it turns out, for much smaller coupling strengths, means that the dynamic behavior of the waterwheel is consistent with the Lorenz model, at least within the given experimental limitations. The observed synchronization does not necessarily imply that the Lorenz equations are the correct model, but the presented data provide strong evidence that the Lorenz model is a good description.

VI. DISCUSSION

We have provided details on an inexpensive realization of the Malkus waterwheel and demonstrated that it produces chaotic and periodic behavior as predicted theoretically. We also showed that a numeric model implementing the Lorenz equations synchronizes to the wheel's chaotic motion with surprisingly good quality. We discussed how chaos synchronization can be used to test whether the wheel dynamics is consistent with the Lorenz model. We find that, within the limitations of an experimental system, the Lorenz model appears to provide a good description of the water wheel dynamics.

No model of a real system can be perfect and noise is present in any measurement. It is, therefore, not surprising that we find small differences between the experimental data and theoretical model. The interesting question and open challenge is to develop tools that allow one to determine the main source of the remaining error, which could be due to noise, parameter mismatches, or structural insufficiencies of the model.

Perfect chaos synchronization between two (noise-free) chaotic systems is only achievable if the master system and the driven system are identical. One might, therefore, suspect that the parameters used in the simulations do not correspond perfectly to the wheel's operating condition because there is uncertainty in the experimentally determined parameter values. Stated another way, one is confronted with the problem of finding the true parameter values of a chaotic model based solely on ones knowledge of a single scalar time series from an experiment, in this case $\theta(t)$. This is a difficult problem due to the sensitive dependence of chaotic systems on the parameters and initial conditions of the unknown state variables (y and z). Recently, proposed techniques, inspired by control engineering approaches, are in some cases able to solve this problem.[29–32] Utilizing these ideas, we designed an adaptive observer[29] that generates for a given time series an estimate of the corresponding model parameter values. These estimates are optimal in the sense that they are guaranteed to converge to the correct values as long as the Lorenz model is a precise description of the waterwheel dynamics and noise is entirely due to unbiased measurement noise. It is these optimized values that were used for all simulation results shown in this paper. A detailed discussion of the adaptive observer technique is beyond the scope of this paper. However, we note that the optimized parameter values are in close correspondence to the estimates based on the experimental measurements. For the chaotic time series shown in Fig. 5(b), the optimized values are $\sigma \approx 2.5$ and $\rho \approx 66$, as compared with the experimentally determined values of $\sigma \approx 2.7$ and $\rho \approx 69$. Given the measurement uncertainties, we find this close correspondence rather surprising.

In summary, of the three potential causes for the differences between the experimental data and the theoretical model—noise, parameter mismatches, and structural insufficiencies of the model—we can exclude parameter mismatches. We do know that there is noise in the experimental data that contributes to the observed differences. We cannot exclude model insufficiencies but if they exist their effect must be small. Thus, we believe that the waterwheel described in this paper comes close to an ideal one, one whose dynamics is exactly described by the Lorenz equations. This system can, therefore, be used to explore other interesting aspects of the Lorenz system, such as its bifurcations.

ACKNOWLEDGMENTS

This work was supported by the Research Corporation for Science Advancement (Award No. 7847). The authors thank Greg Eibel for helping with the construction of the wheel, Jay Ewing for help with the video analysis, and Adarsh Pyrelal for initial tests aimed at characterizing the wheel parameters. L.I. thanks the nonlinear dynamics group at Redstone Arsenal, Huntsville for their hospitality and inspiring conversations.

APPENDIX A: NUMERIC CALCULATION OF THE LYAPUNOV EXPONENTS

For completeness, we present in this section the definition of Lyapunov exponents and provide some details on how to compute them numerically. Some reviews on this topic are found in Wolf *et al.*,[33] Geist *et al.*,[34] and Souza-Machado *et al.*[35]

The object of study is a system of nonlinear ordinary differential equations,

$$\dot{\mathbf{x}} = \mathbf{f}(\mathbf{x}), \quad \mathbf{x}(0) = \mathbf{x}_0, \tag{A1}$$

where $\mathbf{x}(t) = (x_1(t), x_2(t), \ldots, x_n(t)) \in \mathbb{R}^n$, $\mathbf{x}_0$ is the initial condition, and $\mathbf{f}$ is an n-dimensional vector field. To define Lyapunov exponents associated with solutions $\mathbf{x}(t)$, one needs to take into account that the rate of separation of two trajectories in phase space can be different for different orientations of the initial separation vector. Therefore, one has to consider a spectrum of n Lyapunov exponents for an n dimensional phase space $\{\lambda_1, \lambda_2, \ldots, \lambda_n\}$. Since the Lyapunov spectrum characterizes the evolution of infinitesimal perturbations, one can utilize a linearization around a fiduciary trajectory via solutions to the matrix differential equation

$$\dot{\mathbf{Y}} = \mathbf{J}\,\mathbf{Y}; \quad \mathbf{Y}(\mathbf{x}_0, t = 0) = \mathbb{1}. \tag{A2}$$

In this equation, $\mathbf{J}$ is the time-dependent Jacobian matrix with elements $\mathbf{J}_{ij}[\mathbf{x}(t)] = (\partial f_i/\partial x_j)|_{\mathbf{x}=\mathbf{x}(t)}$ that are the partial derivatives of the vector field $\mathbf{f}$ in Eq. (A1) evaluated along the fiduciary trajectory $\mathbf{x}(t)$. With the identity matrix as initial condition the $n \times n$ matrix $\mathbf{Y}$ then gives the complete linearized flow map with respect to the standard orthonormal basis $\{\hat{\mathbf{e}}_1, \ldots, \hat{\mathbf{e}}_n\}$. In other words, $\mathbf{Y}(\mathbf{x}_0, t)$ describes the evolution in time of both the magnitude and the orientation in phase space of any initial infinitesimal perturbation from $\mathbf{x}_0$ because $\delta\mathbf{x}(t) = \mathbf{Y}(\mathbf{x}_0, t)\delta\mathbf{x}_0$. The Lyapunov exponents λ_i are defined by the logarithms of the (real) eigenvalues μ_i of the positive and symmetric matrix

$$\Lambda = \lim_{t\to\infty} \left[\mathbf{Y}^{\mathrm{T}}(\mathbf{x}_0, t)\mathbf{Y}(\mathbf{x}_0, t)\right]^{1/2t}, \tag{A3}$$

where $\mathbf{Y}^{\mathrm{T}}$ $(\mathbf{x}_0, t)$ denotes the transpose of $\mathbf{Y}(\mathbf{x}_0, t)$. This implies that for every initial condition $\mathbf{x}_0$ there exists an orthonormal set of initial perturbation vectors $\delta\mathbf{v}_i$ such that

$$\lambda_i = \lim_{t\to\infty} \frac{1}{t} \ln|\mathbf{Y}(\mathbf{x}_0, t)\delta\mathbf{v}_i|, \quad i = 1, 2, \ldots, n. \tag{A4}$$

It was shown by Oseledets[36] that the limits on the right-hand side of Eqs. (A3) and (A4) exist for almost every initial condition $\mathbf{x}_0$, and it has been argued[37] that for ergodic systems the values of the Lyapunov exponents $\{\lambda_i\}$ do not depend on the initial conditions (up to a measure zero in phase space). Thus, the Lyapunov exponents are global properties of the attractor of the dynamical system.

The definition of the Lyapunov exponents might suggest that we should integrate the linearized equation (A2) along with the nonlinear differential equation (A1). This is not feasible because the exponential growth and decay rates of initial perturbation vectors quickly exceed the capabilities of numerical number representation in a computer. Furthermore, perturbation vectors quickly align with the direction of maximal growth making it impossible to determine any but the largest Lyapunov exponent. To compute the Lyapunov spectrum, the most commonly used algorithms are based on a step-wise procedure where Eq. (A2) is integrated for short intervals of time and the vectors spanning the phase space volume are reorthonormalized at each step.

To be precise, we compute the largest k Lyapunov exponents by considering the evolution of the volume V_k of k-dimensional parallelepipeds in n-dimensional phase space. It can be shown that V_k is given in terms of the sum of the largest k Lyapunov exponents[38,39] via

$$\sum_{i=1}^{k} \lambda_k = \lim_{t\to\infty} \frac{1}{t} \ln[V_k] \quad (1 \le k \le n), \tag{A5}$$

when the λ_i form a monotonically decreasing sequence. Consider, therefore, an initial k-dimensional hypercube centered on the initial point $\mathbf{x}_0$, where the cube is defined via an orthogonal $n \times k$ matrix $\mathbf{P}_0 = (\hat{\mathbf{o}}_1, \ldots, \hat{\mathbf{o}}_k)$, the columns of which are k (randomly chosen) orthonormal n-dimensional vectors $\hat{\mathbf{o}}_i$ forming the cube's axes. Under the action of the flow the cube will deform into a parallelepiped $\mathbf{P}(t) = \mathbf{Y}(\mathbf{x}_0, t)\mathbf{P}(0)$ with volume V_k. The volumes V_k can be computed via the QR decomposition[40] that factorizes an $n \times k$ matrix $\mathbf{P} = \mathbf{QR}$ into the product of an orthogonal $n \times k$ matrix $\mathbf{Q}$ and an upper triangular $k \times k$ matrix $\mathbf{R}$ with positive diagonal elements R_{ii}. The volume of $\mathbf{P}$ is thus

$$V_k = |\det \mathbf{P}| = |\det \mathbf{R}| = \prod_{i=1}^{k} R_{ii}. \tag{A6}$$

Substituting this expression into Eq. (A5) for V_k for all k with $1 \le k \le n$, we find that

$$\lambda_i = \lim_{t\to\infty} \frac{1}{t} \ln[R_{ii}(t)] \quad (i = 1, \ldots, k). \tag{A7}$$

We can calculate the time average of the R_{ii} in Eq. (A7) in a stable manner. To do so, first note that the evolution in time of $\mathbf{P}$ is given by

$$\frac{d\mathbf{P}}{dt} = \frac{d\mathbf{Y}}{dt}\mathbf{P}(0) = \mathbf{J}\mathbf{P}(t). \tag{A8}$$

The advantage of considering the time evolution of $\mathbf{P}$ is that the determination of the largest k Lypunov exponents involves the integration of just $n(1+k)$ differential equations instead of the $n(1+n)$ equations that would be necessary if one considered the evolution of $\mathbf{Y}$. The computation proceeds stepwise, where one integrates over a sufficiently small time-interval $\Delta t_j = t_j - t_{j-1}$, the coupled differential equations

$$\begin{aligned} &\frac{d\mathbf{x}}{dt} = \mathbf{f}(\mathbf{x}), \qquad \mathbf{x}(t_{j-1}^{+}) = \mathbf{x}(t_{j-1}^{-}) \\ &\frac{d\mathbf{P}}{dt} = \mathbf{J}[\mathbf{x}(t)]\mathbf{P}, \quad \mathbf{P}(t_{j-1}^{+}) = \mathbf{Q}_{j-1}, \end{aligned} \qquad t_{j-1} \le t \le t_j. \tag{A9}$$

The initial conditions for the first step are $\mathbf{x}(0) = \mathbf{x}_0$ and $\mathbf{P}(0) = \mathbf{P}_0$. The size of the time step Δt_j has to be chosen such that $\mathbf{P}(t)$ remains well conditioned. Time steps on the order of a typical oscillation period are often suggested. Next, the QR decomposition of the matrix $\mathbf{P}_j = \mathbf{P}(t_j)$ (Fig. 7),

$$\mathbf{P}_j = \mathbf{Q}_j\mathbf{R}_j, \tag{A10}$$

is performed to reorthonormalize the phase space volume. The orthogonal matrix $\mathbf{Q}_j$ is used to initialize the integration of the next step and the diagonal matrix elements of $\mathbf{R}_j$ are accumulated to compute the Lyapunov exponents. Since the flow matrix $\mathbf{P} = \mathbf{P}_m \cdots \mathbf{P}_0$ can be expressed as the product of the matrices $\mathbf{P}_j$ computed at successive points along the orbit $\mathbf{x}(t_j)$, the above procedure implies that

$$\mathbf{P} = \mathbf{Q}_m\mathbf{R}_m\mathbf{R}_{m-1} \cdots \mathbf{R}_1. \tag{A11}$$

Thus, the Lyapunov exponents are

$$\lambda_i = \lim_{m\to\infty} \frac{\sum_{j=1}^{m} \ln[R_{ii,j}]}{\sum_{j=1}^{m} \Delta t_j}. \tag{A12}$$

We implement the above procedure using an adaptive stepsize integrator (the DDRIV fortran-integrator) and the QR decomposition routine contained in the LAPACK library.

In general the convergence to the limit in Eq. (A12) is very slow and it is useful to have checks on how well the exponents have been approximated. To do so, we note that for a dissipative system, such as the Lorenz system, the total phase space volume contracts (exponentially in time on average), implying that the sum of all Lyapunov exponents,

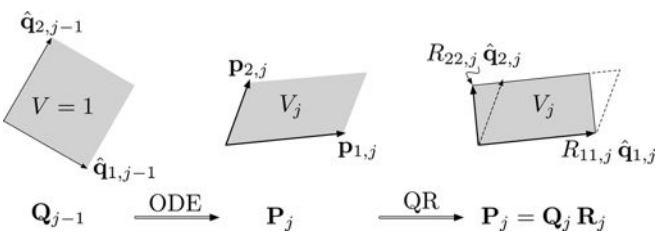

Fig. 7. Geometric illustration of the QR decomposition scheme for computing Lyapunov exponents.

$$\sum_{i=1}^{3}\lambda_i = \lim_{t\to\infty}\frac{1}{t}\ln|\det\mathbf{Y}| = \lim_{t\to\infty}\frac{1}{t}\ln[V_3(t)], \tag{A13}$$

must be negative. For the Lorenz system with $b=1$ [Eq. (22)] with corresponding linearized flow equation

$$\dot{\mathbf{Y}} = \mathbf{J}\mathbf{Y}, \qquad \mathbf{J} = \begin{pmatrix} -\sigma & \sigma & 0 \\ \rho - z & -1 & -x \\ y & x & -1 \end{pmatrix}, \tag{A14}$$

One can calculate the phase space volume contraction rate explicitly by applying Liouville's formula to Eq. (A14):

$$\det\mathbf{Y}(\mathbf{x}_0,t) = \det\mathbf{Y}(\mathbf{x}_0,0)\exp\left(\int_0^t \mathrm{tr}[\mathbf{J}(\xi)]\mathrm{d}\xi\right). \tag{A15}$$

Since $\det\mathbf{Y}(\mathbf{x}_0,0) = \det\mathbb{1} = 1$ and the trace of the Jacobian is a constant ($\mathrm{tr}[\mathbf{J}] = -\sigma - 2$), Eq. (A13) implies that

$$\sum_{i=1}^{3}\lambda_i = \lim_{t\to\infty}\frac{1}{t}\int_0^t \mathrm{tr}[\mathbf{J}(\xi)]\mathrm{d}\xi = -\sigma - 2. \tag{A16}$$

This provides a cross-check for convergence. A second check is obtained by noting that perturbations along a trajectory will neither grow nor shrink exponentially in time, implying that there is a zero Lyapunov exponent. This zero exponent exists whenever the attractor is not a fixed point, e.g. for periodic or chaotic dynamics.

We utilize these checks in our numerical procedure by computing all three Lyapunov exponents for the Lorenz system and accepting the computed values whenever (a) the zero exponent, if it exists, has converged such that its magnitude is smaller than 10^{-3} and (b) the sum condition (A16) is satisfied to within $\left|-(2+\sigma) - \sum_{i=1}^{3}\lambda_i\right| < 10^{-3}$.

APPENDIX B: PROVING SYNCHRONIZATION

To begin, note that exactly synchronized solutions of the coupled systems (22) and (26) correspond to a zero error-vector $\mathbf{e}(t)=0$, where the components of $\mathbf{e}$ are defined as $(e_x,e_y,e_z) = (x_\mathrm{m}-x, y_\mathrm{m}-y, z_\mathrm{m}-z)$. It is, therefore, convenient to consider the evolution of $\mathbf{e}$, which is described by a non-autonomous ordinary differential equation of the form $\dot{\mathbf{e}} = \mathbf{F}(\mathbf{e},t)$, given by

$$\begin{aligned} \dot{e}_x &= \sigma(e_y - e_x) - Ke_x \\ \dot{e}_y &= \rho e_x - e_y - e_x e_z - x(t)e_z - z(t)e_x \\ \dot{e}_z &= e_x e_y - e_z + x(t)e_y + y(t)e_x. \end{aligned} \tag{B1}$$

Solutions $\mathbf{e}(t)$ can be thought of as trajectories in a three-dimensional phase space. To prove synchronization, we need to show that for any initial condition the corresponding solution trajectory asymptotically approaches the origin of this phase space: $\mathbf{e}\to 0$ as $t\to\infty$. Since the solutions of the Lorenz equations enter into Eq. (B1), it is useful to establish bounds for the Lorenz solutions. Bounds can be obtained by constructing a trapping region—a closed region in the phase space of Eq. (22) with the property that solutions starting on the inside of this region never leave, and solutions starting on the outside will eventually enter. For the Lorenz equations with $b=1$, the following inequalities define a trapping region[41]

$$x^2 < 4\sigma\rho \; y^2 \le \rho^2 \; 0 \le z \le 2\rho, \tag{B2}$$

for positive real-valued parameters σ and ρ.

Next, we utilize a function that decreases along trajectories of system (B1), a so-called Lyapunov function. As a Lyapunov function candidate consider the scalar function

$$V(\mathbf{e}) = \frac{e_x^2 + e_y^2 + e_z^2}{2}, \tag{B3}$$

which is positive definite for $\mathbf{e}\neq 0$, zero for $\mathbf{e}=0$, and monotonically increasing as a function of $|\mathbf{e}|$. If we can show that $\dot{V}<0$ for all $\mathbf{e}\neq 0$, then all trajectories flow "downhill" toward the origin and $\mathbf{e}=0$ is globally asymptotically stable.[11] Using Eq. (B1) we obtain

$$\begin{aligned} \dot{V}(\mathbf{e}) &= e_x\dot{e}_x + e_y\dot{e}_y + e_z\dot{e}_z \\ &= -\left[K + \sigma - \frac{(\sigma+\rho-z)^2}{4} - \frac{y^2}{4}\right]e_x^2 \\ &\quad - \left(e_y - \frac{\sigma+\rho-z}{2}e_x\right)^2 - \left(e_z - \frac{y}{2}e_x\right)^2, \end{aligned} \tag{B4}$$

for the time derivative of V. Utilizing Eq. (B2), a lower bound for the expression in the square brackets is found in terms of the time-independent parameters ρ and σ as

$$K + \sigma - \frac{(\sigma+\rho-z)^2}{4} - \frac{y^2}{4} \ge K + \sigma - \frac{(\sigma+\rho)^2}{4} - \frac{\rho^2}{4}. \tag{B5}$$

This equation then shows that for sufficiently large coupling strengths K,

$$4K > \sigma^2 + 2\sigma\rho + 2\rho^2 - 4\sigma, \tag{B6}$$

the expression in square brackets in the first term of Eq. (B4) is positive definite. It then follows from Eq. (B4) that

$$\dot{V}(\mathbf{e}) < 0 \quad \forall\mathbf{e}\neq 0, \tag{B7}$$

concluding the proof.

[a]Electronic mail: illing@reed.edu

[1]E. N. Lorenz, "Deterministic nonperiodic flow," J. Atmos. Sci. **20**, 130–141 (1963).
[2]K. Dreyer and F. R. Hickey, "The route to chaos in a dripping water faucet," Am. J. Phys. **59**, 619–627 (1991).
[3]N. J. Corron, S. D. Pethel, and B. A. Hopper, "Controlling chaos with simple limiters," Phys. Rev. Lett. **84**, 3835–3838 (2000).
[4]R. A. Schmitz, K. R. Graziani, and J. L. Hudson, "Experimental evidence of chaotic states in the Belousov-Zhabotinskii reaction," J. Chem. Phys. **67**, 3040–3044 (1977).
[5]L. Illing, D. J. Gauthier, and R. Roy, *Advances in Atomic, Molecular, and Optical Physics*, edited by P. R. Berman, E. Arimondo, and C. Lin (Elsevier, Amsterdam, 2007), vol. 54, pp. 615–695.
[6]A. Argyris, D. Syvridis, L. Larger, V. Annovazzi-Lodi, P. Colet, I. Fischer, J. Garcia-Ojalvo, C. R. Mirasso, L. Pesquera, and K. A. Shore, "Chaos-based communications at high bit rates using commercial fibre-optic links," Nature (London) **438**, 343–346 (2005).

[7]H. L. D. d. S. Cavalcante, D. J. Gauthier, J. E. S. Socolar, and R. Zhang, "On the origin of chaos in autonomous Booleannetworks," Philos. Trans. R. Soc. London, Ser. A. A **368**, 495–513 (2010).
[8]K. E. Callan, L. Illing, Z. Gao, D. J. Gauthier, and E. Schöll, "Broadband chaos generated by an optoelectronic oscillator," Phys. Rev. Lett. **104**, 113901 (2010).
[9]E. N. Lorenz, *The Essence of Chaos* (University of Washington Press, Seattle, WA, 1993).
[10]W. V. R. Malkus, "Non-periodic convection at high and low Prandtl number," Mem. Soc. R. Sci. Liege Collect. in-4, 125–128 (1972).
[11]S. H. Strogatz, *Nonlinear Dynamics and Chaos* (Addison-Wesley, Reading, MA, 1994).
[12]J. L. Tylee, "Chaos in a real system," Simulation **64**, 176–183 (1995).
[13]H. D. Wiederick, N. Gauthier, D. A. Campbell, and P. Rochon, "Magnetic braking: Simple theory and experiment," Am. J. Phys. **55**, 500–503 (1987).
[14]M. A. Heald, "Magnetic braking: Improved theory," Am. J. Phys. **56**, 521–522 (1988).
[15]M. Marcuso, R. Gass, D. Jones, and C. Rowlett, "Magnetic drag in the quasi-static limit: A computational method," Am. J. Phys. **59**, 1118–1123 (1991).
[16]Since one can assume the air drag to be linear in the angular velocity, it is included in this analysis and contributes to κ.
[17]L. E. Matson, "The Malkus–Lorenz water wheel revisited," Am. J. Phys. **75**, 1114–1122 (2007).
[18]We use Loc-Line hoses and nozzles.
[19]DigiFlow 8000T.
[20]D. Pnueli and C. Gutfinger, *Fluid Mechanics* (Cambridge University Press, 1992).
[21]C. Sparrow, *The Lorenz Equations: Bifurcations, Chaos and Strange Attractors* (Springer-Verlag, New York, 1982).
[22]Z. Galias and P. Zgliczynski, "Computer assisted proof of chaos in the Lorenz equations," Physica D **115**, 165–188 (1998).
[23]W. Tucker, "The Lorenz attractor exists," C. R. Acad. Sci. Ser. I: Math. **328**, 1197–1202 (1999).
[24]K. Mischaikow, M. Mrozek, and A. Szymczak, "Chaos in the Lorenz equations: A computer assisted proof part III: Classical parameter values," J. Diff. Eqs. **169**, 17–56 (2001).
[25]H. D. I. Abarbanel, *Analysis of Observed Chaotic Data* (Springer, New York, 1995).
[26]H. Kantz and T. Schreiber, *Nonlinear Time Series Analysis* (Cambridge U.P., Cambridge, 2004).
[27]A. Pikovsky, M. Rosenblum, and J. Kurths, *Synchronization: A Universal Concept in Nonlinear Sciences* (Cambridge U.P., Cambridge, 2003).
[28]Chaos synchronization was independently discovered three times: by H. Fujisaka and T. Yamada in Japan [Prog. Theor. Phys. **69**, 32–47 (1983)], by V. S. Afraimovich, N. N. Verichev, and M. I. Rabinovich in the USSR [Radiophys. Quantum Electron. **29**, 795–803 (1986)], and by L. M. Pecora and T. L. Carroll in the US [Phys. Rev. Lett. **64**, 821–824 (1990)].
[29]B. R. Andrievskii, V. O. Nikiforov, and A. L. Fradkov, "Adaptive observer-based synchronization of the nonlinear nonpassifiable systems," Autom. Remote Control **68**, 1186–1200 (2007).
[30]D. C. Yu and U. Parlitz, "Estimating parameters by autosynchronization with dynamics restrictions," Phys. Rev. E **77**, 066221 (2008).
[31]F. Sorrentino and E. Ott, "Using synchronization of chaos to identify the dynamics of unknown systems," Chaos **19**, 033108 (2009).
[32]H. D. I. Abarbanel, M. Kostuk, and W. Whartenby, "Data assimilation with regularized nonlinear instabilities," Q. J. R. Meteorol. Soc. **136**, 769–783 (2010).
[33]A. Wolf, J. B. Swift, H. L. Swinney, and J. A. Vastano, "Determining Lyapunov exponents from a time-series," Physica D **16**, 285–317 (1985).
[34]K. Geist, U. Parlitz, and W. Lauterborn, "Comparison of different methods for computing Lyapunov exponents," Prog. Theor. Phys. **83**, 875–893 (1990).
[35]S. D. Souza-Machado, R. W. Rollins, D. T. Jacobs, and J. L. Hartman, "Studying chaotic systems using microcomputer simulations and Lyapunov exponents," Am. J. Phys. **58**, 321–329 (1990).
[36]V. I. Oseledets, "A multiplicative ergodic theorem. Lyapunov characteristic numbers for dynamical systems," Trans. Moscow Math. Soc. **19**, 197–231 (1968).
[37]J. D. Farmer, E. Ott, and J. A. Yorke, "The Dimension of chaotic attractors," Physica D **7**, 153–180 (1983).
[38]G. Benettin, L. Galgani, A. Giorgilli, and J. M. Strelcyn, "Lyapunov characteristic exponents for smooth dynamical systems and for Hamiltonian systems; A method for computing all of them, Part 1: Theory," Meccanica **9**, 9–20 (1980).
[39]G. Benettin, L. Galgani, A. Giorgilli, and J. M. Strelcyn, "Lyapunov characteristic exponents for smooth dynamical systems and for Hamiltonian systems; A method for computing all of them, Part 2: Numerical Application," Meccanica **9**, 21–30 (1980).
[40]G. H. Golub and C. F. Van Loan, *Matrix Computations* (Johns Hopkins U.P., Baltimore, 1996).
[41]P. Swinnerton-Dyer, "Bounds for trajectories of the Lorenz equations: An illustration of how to choose Liapunov functions," Phys. Lett. A **281**, 161–167 (2001).